Satellite-derived global surface water extent and dynamics over the last 25 years (GIEMS-2)

C. Prigent, C. Jimenez, Philippe Bousquet

HAL Id: insu-03660253

https://insu.hal.science/insu-03660253

Submitted on 5 May 2022

Correspondence to:
C. Prigent,
catherine.prigent@obspm.fr

Satellite-Derived Global Surface Water Extent and Dynamics Over the Last 25 Years (GIEMS-2)

C. Prigent[1,2] [ID], **C. Jimenez[2,1]** [ID], and **P. Bousquet[3]** [ID]

[1]Sorbonne Université, Observatoire de Paris, Université PSL, CNRS, LERMA, Paris, France, [2]Estellus, Paris, France, [3]Laboratoire des Sciences du Climat et de l'Environnement, CEA/CNRS/UVSQ, Université Paris Saclay, GifsurYvette, France

Abstract A method has been developed to extend the Global Inundation Estimate from Multiple Satellites (GIEMS). The method presented here is based on retrieval principals similar to GIEMS but with an updated estimation of microwave emissivity in order to be less dependent on ancillary data and with some changes to the final surface water estimation to correct a known overestimation over low vegetation areas. The new methodology, GIEMS-2, provides monthly estimates of surface water extent, including open water, wetlands, or rice paddies, and it has been applied to the Special Sensor Microwave/Imager and the Special Sensor Microwave Imager Sounder intercalibrated observations to produce a global data record of surface water extent from 1992 to 2015, on an equal area grid of 0.25° × 0.25° at the equator (~25 km). The time series have been thoroughly evaluated: they are seamless and do not show any obvious artifact related to changes in satellite instrumentation over the ~25 years. Comparisons with precipitation estimates show good agreement, displaying expected patterns related to surface conditions and precipitation regimes. The temporal variability of basin-averaged estimates has also been compared with altimeter river height, showing a reasonable agreement. Production will be continued up to current time as soon as the observations become available, with efforts to improve the spatial and temporal resolutions of the estimates currently underway.

Plain Language Summary A method has been developed to provide global estimates of the continental surface waters and their dynamics. It comprises all surface waters, including open water, wetlands, or rice paddies. With multiple satellite data, a global data record of surface water extent is produced, on a monthly basis from 1992 to 2015, with a spatial resolution of 25 km. The time series have been thoroughly evaluated: They are seamless and do not show any obvious artifact related to changes in satellite instrumentation over the 25 years. Comparisons with precipitation estimates show good agreement, displaying expected patterns related to surface conditions and precipitation regimes. Temporal variability of basin-averaged estimates has also been compared with altimeter river height, showing a reasonable agreement. Production will be continued up to current time as soon as carefully intercalibrated satellite observations become available, with efforts to improve the spatial and temporal resolution of the estimates currently underway.

1. Introduction

Terrestrial surface waters encompass a large variety of environments, from exceptionally flooded populated areas and their related human loss to rice paddies to feed the populations, tropical wetlands very rich in biodiversity, or climate-sensitive boreal peat land with their large methane emission. Mapping of surface waters is required for a wide range of applications, some needing global low spatial resolution with long-term objectives and others favoring high spatial resolution and temporal sampling with almost real-time observations. At low spatial resolution, the surface water extent and their dynamics are key information to model Earth hydrological and biochemical cycles. Long time series of global surface water estimates are necessary today to analyze the changes in the wetland-related methane emission (e.g., Melton et al., 2013; Wania et al., 2013), and climate modelers are in strong need of wetland extent information to understand the methane variability over past decades (e.g., Kirschke et al., 2013; Pison et al., 2013; Ringeval et al., 2010) for a better prediction of its evolution in the upcoming decades (e.g., Nisbet et al., 2018; Saunois et al., 2017).

Despite their importance, the global distribution of the surface waters and their dynamics are still not consolidated, especially at global scale and for long time periods. The potential of satellite Earth observations for the mapping of surface waters has already been exploited (for reviews see Alsdorf et al., 2007; Prigent et al., 2016). Satellite observations in the visible, infrared, or microwave domains have the potential to detect surface water extent and their variations, with different degrees of success depending on the environments. Optical and near-infrared satellite measurements provide good spatial resolutions but are limited by their inability to penetrate clouds and dense vegetation. For instance, with the processing of a large volume of Landsat satellite data, Pekel et al. (2016) proposed a global data set at 30 m, including the description of the dynamics and probability of occurrence over 30 years. These estimates cover open water bodies but exclude wetlands that are vegetated. Microwaves, passive or active, can penetrate clouds and vegetation to a certain extent. With the Synthetic Aperture Radar (SAR), high spatial resolution is obtained even under cloudy condition, as demonstrated by Santoro et al. (2015) using Envisat instrument or by Pham-Duc, Prigent, and Aires et al. (2017) using the Sentinel-1 mission. However, global SAR products describing the surface water dynamics are not available yet. Passive microwave observations have long been used to detect surface water extents, despite their low spatial resolution. However, used alone, it is difficult to subtract the vegetation contribution from the measured signal.

A methodology was developed to estimate the extent and dynamics of surface waters at the global scale, combining passive and active microwaves, along with visible and near-infrared observations (Papa et al., 2010; Prigent, Matthews et al., 2001; Prigent et al., 2007, 2012). These multiple-satellite data have different sensitivities to surface properties (e.g., vegetation, topography, soil properties), and their combined use makes it possible to disentangle the contributions of the various factors in the observations. A monthly estimate of surface water extents was produced for 1993–2007, with a 0.25° × 0.25° spatial resolution: the Global Inundation Extent from Multiple Satellites (GIEMS). Note that another multisatellite product was generated recently, also based on the merging of passive and active microwave satellite observations, the Surface Water Microwave Product Series (SWAMPS) (Schroeder et al., 2015), but it showed significant limitations (Pham-DucPham-Duc, Prigent, Aires, & Papa et al., 2017).

The initial version of GIEMS will be called GIEMS-1 in this study. The following satellite observations were used: (1) passive microwave measurements between 19 and 85 GHz from the Special Sensor Microwave/Imager (SSM/I) on board the Defense Meteorological Satellite Program (DMSP) polar orbiters; (2) active microwave backscattering coefficients at 5.25 GHz from scatterometers, and; (3) visible and near-infrared reflectances and the derived Normalized Difference Vegetation Index (NDVI). The algorithm was a three-step process (Figure 1). First, a preprocessing was applied to the passive microwave observations to calculate the land surface microwave emissivity. It suppressed the modulation of the microwave observations by the surface temperature and the atmospheric effects. It required significant amount of ancillary data to describe the surface temperature and the atmospheric parameters. Ancillary data were provided by the International Satellite Cloud Climatology Project (ISCCP, Rossow & Schiffer, 1999) and the National Centers for Environmental Prediction National Center for Atmospheric Research (NCEP-NCAR) reanalyses. The second step consisted in merging the three sources of satellite information and to apply an unsupervised clustering algorithm to identify the inundated pixels. Third step, for each pixel where surface water was detected, the fractional surface water extent was calculated. The emissivity polarization difference at 37 GHz is particularly sensitive to the surface water fraction, but this signal is modulated by the presence of vegetation. A linear mixing model was applied, using the active microwave backscattering coefficient as a proxy for vegetation. The technique was globally applicable without tuning for specific environments.

The GIEMS-1 essential information, the passive microwaves from the conical scanners SSM/I and Special Sensor Microwave Imager Sounder (SSMIS), are available since 1992 up to current time. These observations have recently been intercalibrated at the Climate Satellite Application Facility (Climate SAF) under EUMETSAT support up to 2015 and are provided to the community with a quality compatible with climate applications (Fennig et al., 2017). GIEMS-1 also required key ancillary data, and to obtain a climate quality data set, these data had to be of similar provenance and of constant quality over time. This was an issue for GIEMS-1, as the production of the ISCCP data that provided the surface temperature and the cloud flags was interrupted for some years, preventing the calculation of the estimates after 2008.

An alternative methodology is thus developed here to calculate the surface water extent and dynamics over the 25 years and to make it possible to update the data set in the future. It requires fewer input parameters,
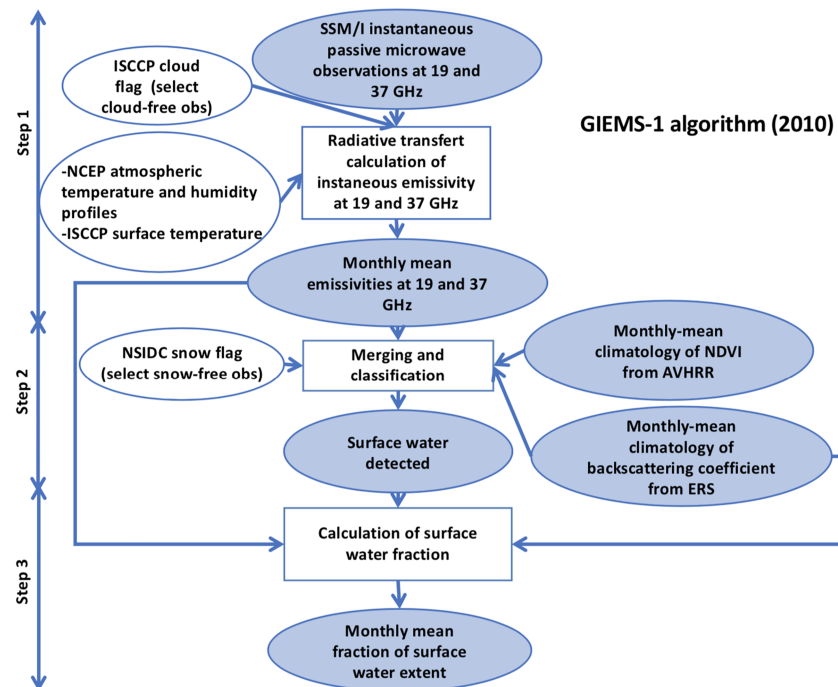
Figure 1. Schematic presentation of the original GIEMS-1 algorithm.

while producing estimates of equivalent quality and compatible with the products previously distributed, used, and validated. Section 2 presents the new methodology and provides comparisons with the former one. The data production over the 1992–2015 period is described, insisting on the challenge of deriving long-term climate quality products using observations from a succession of different satellite instruments (section 3). In section 4, the satellite-derived surface water extents are evaluated by comparisons with related hydrological information, namely, precipitation and altimetric river height. Section 5 summarizes this study.

2. An Updated Methodology to Estimate Surface Water Extent, With a Limited Number of Data Inputs

The main objective of the new methodology is to avoid the use of ancillary data whose production can be interrupted or that can experience discontinuities due to sensor and/or algorithm changes. Here, we describe the algorithmic and input data changes: the new passive microwave emissivity calculation (first step), the detection of the inundated pixels (second step), and the updated quantification of the surface water fraction per pixel (third step). Changes in the emissivity estimation in the first step were required in order to reduce the number of ancillary data and are described in section 2.1. The second step is unchanged, except for the snow flag that is now derived from reanalyses as detailed in section 2.2. Regarding the third step, GIEMS-1 users mentioned at several occasions that over low vegetation (e.g., croplands such as rice paddies, open shrublands, and grasslands when flooded), the surface water was overestimated, especially in Southeast Asia (e.g., over the Ganges and Bramahputra basins (Papa et al., 2015)). As a consequence, a solution is proposed in section 2.3 to calculate the fractional water coverage for each pixel, after the water detection (Step 3 in Figure 1). A schematic presentation of the new GIEMS-2 algorithm is provided in Figure 2. The changes from the GIEMS-1 methodology (Figure 1) are indicated in red.

2.1. Emissivity Calculation

A key indicator of the water presence is provided by the passive microwave land surface emissivity that strongly decreases in presence of water (Step 1 in Figure 1). The microwave emissivity was initially derived from the satellite observations (the microwave brightness temperatures Tbs), under clear sky conditions, subtracting the contribution from the atmosphere and the surface using radiative transfer calculation (Aires et al., 2001; Prigent et al., 1997). Atmospheric reanalyses from NCEP provided the necessary information
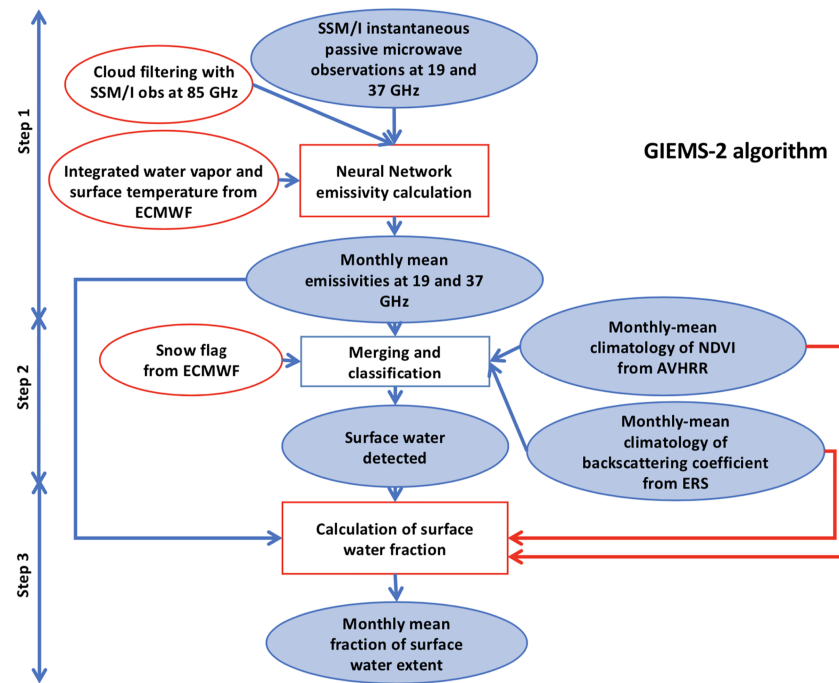
Figure 2. Schematic presentation of the GIEMS-2 algorithm. The changes from GIEMS-1 methodology are indicated in red.

to estimate the clear sky atmospheric contribution from radiative transfer calculation. The surface skin temperatures and the cloud flags were extracted from the ISCCP data set.

A new method is proposed here to estimate the microwave emissivity, based essentially on the direct measurements from passive microwave conical imagers at 19 and 37 GHz in both perpendicular polarizations, with limited inputs from Numerical Weather Prediction reanalysis. In GIEMS-1, the full atmospheric profiles from NCEP reanalyses were adopted to produce the emissivities, along with cloud parameters and surface skin temperature from ISCCP. Here, a limited number of parameters from the ECMWF reanalysis ERA-INTERIM are collected (Dee et al., 2011), to help constrain the emissivity estimation (namely, the surface skin temperature and the integrated water vapor). The ERA-INTERIM data are available from 1979 to current time, with consistency over the full period for climate applications. Concerning the clouds, the high-frequency microwave observations contain information on the cloud presence, with the highest SSM/I frequency at 85 GHz being particularly sensitive to the presence of convective clouds that can obscure the surface properties and hamper the surface emissivity estimation. Although the GIEMS-1 and -2 processing only relies on the 19 and 37 GHz emissivities, which are much less sensitive to cloud presence, careful analysis of the 85 GHz Tbs is used to derive an internal cloud flag to help filter out the SSM/I observations contaminated by deep clouds in the new processing.

The new method is based on a statistical inversion of the microwave brightness temperatures (Tbs) to directly estimate the microwave emissivity, avoiding the use of radiative transfer calculation and a large set of ancillary data. Neural network (NN) regressions have already been developed successfully in many remote sensing applications (e.g., Aires et al., 2001, 2011). A NN methodology is also adopted here, to reproduce the surface emissivity at 19 and 37 GHz, both vertical (V) and horizontal (H) polarizations, using as inputs the seven SSM/I Tbs from 19 to 85 GHz, along with the coincident ECMWF integrated water vapor content and surface skin temperature. The NN scheme selected here is the MultiLayered Perceptron (MLP) model (Rumelhart et al., 1986). We use one NN for the 19 GHz emissivities providing both the V and H polarizations. For the 37 GHz emissivity, we use a first NN for the V polarization and a second one for the V-H polarization difference. The emissivity polarization difference is a key parameter in the GIEMS retrieval, and directly estimating this variable and the 37 GHz H from this difference improves the surface water estimates. Each NN is defined by the number of input neurons (the seven SSM/I Tbs and the ECMWF integrated water vapor and skin temperature), the number of outputs (in our case one, the emissivity or the emissivity

polarization difference), and the number of neurons in a hidden layer to control the complexity of the NN model. Tests showed that one layer with a sufficiently large number of neurons was enough in our case. The final weights are assigned by a Marquardt-Levenberg back-propagation algorithm (Hagan & Menhaj, 1994), with a cross-validation technique used to monitor the evolution of the training error function and prevent overfitting to the training data set.

The NNs are trained on the emissivity calculations already performed using the radiative transfer calculation and all the ancillary data (Aires et al., 2001; Prigent et al., 1997). One year of instantaneous clear sky emissivity calculation is sampled, along with the corresponding SSM/I Tbs at swath level from the Climate SAF and the corresponding water vapor and skin temperature from the ERA-INTERIM reanalyses. The reanalyses are extracted at 0.25° spatial resolution every 6 hr. For each SSM/I Tb observation, the closest ECMWF grid in space is selected, and the values are linearly interpolated in time between the 6 hr samples.

Several tests were performed in the developing phase of the method. A systematic retrieval of all surface emissivities was clearly not successful. The observations without any surface water were dominating the training database: the surface water observations were not sufficiently represented, and the retrieval of the surface water emissivities were not accurate enough. We thus limited the training database to the locations that were inundated at least 1 month during the 1993–2007 period. This improved the retrieval, but there were still rather large errors for the emissivity ranges that were not sufficiently present in the training data base. It was thus decided to sample the data base in such a way that the emissivity values were uniformly represented over their full range of variability. In addition, to improve the estimation, an ensemble of NNs was trained with slightly different initial conditions, instead of just one NN for the emissivity calculation. Then, the multi-ensemble median value was selected as the emissivity estimation. The resulting emissivities are very close to each other for the majority of inversions. Only for difficult retrieval situations can the ensemble median value improve the emissivity estimation, adding robustness to the methodology.

To avoid the major cloud and rain structures that can significantly affect the 19 and 37 GHz observations, the 85 GHz channel is also analyzed. Large depressions of the 85 GHz Tbs are related to scattering by large cloud ice particles generated in convective clouds. When the Tbs at 85 GHz are significantly colder than the monthly mean temperature (lower than twice the monthly standard deviation from the mean), the coincident observations at 19 and 37 GHz are disregarded, and the emissivities are not calculated. This filtering is efficient. It is applied to the instantaneous emissivity calculation, and it suppresses ~5% of the data. Not any contamination of the emissivity by dense clouds or precipitation has been noticed, even in regions that suffer from persistent cloud cover and precipitation.

The final results for the instantaneous swath emissivity show a root mean square (rms) error at 37 GHz of 0.012 at V polarization, 0.014 at H polarization, and 0.004 for the polarization difference, as compared to the initial full radiative transfer calculation using all the ancillary information. At 19 GHz, the emissivity rms error is respectively 0.011 and 0.012 at V and H polarizations. By construction of the NN method, the estimates are not biased. Note that the theoretical errors estimated from the initial emissivity calculated with the radiative transfer and all the ancillary data sets (see Prigent et al., 1997) are of the same order as the difference between the original and the new emissivity calculations. Tests were also performed without the coincident ECMWF reanalysis data. The results were not significantly different (i.e., an increase of 0.001 in rms for all 19 and 37 channels), but the use of the ECMWF information helps to decrease estimation errors in extreme conditions such as very moist or very dry atmospheres. Given the availability, the reliability, and the continuity of the ECMWF reanalysis, we chose to use it systematically in the processing.

Once the instantaneous land surface emissivities are computed at swath level for a month, they are gridded and temporally averaged to produce monthly mean emissivities on an equal area grid of 0.25° × 0.25° at the equator.

2.2. Detection of the Surface Water Pixels
The second step of the algorithm consists in detecting the inundated pixels, through the merging of the monthly mean microwave land surface emissivities with the active microwave data and the visible/near-infrared observations, to benefit from their different sensitivities to the surface parameters (e.g., surface water presence, vegetation density, soil roughness). An unsupervised classification process makes it possible to isolate the inundated pixels (Prigent, Aires et al., 2001). An 8-year monthly mean climatology of the Earth Remote-Sensing Satellite (ERS) scatterometer data at 5 GHz is adopted, along with
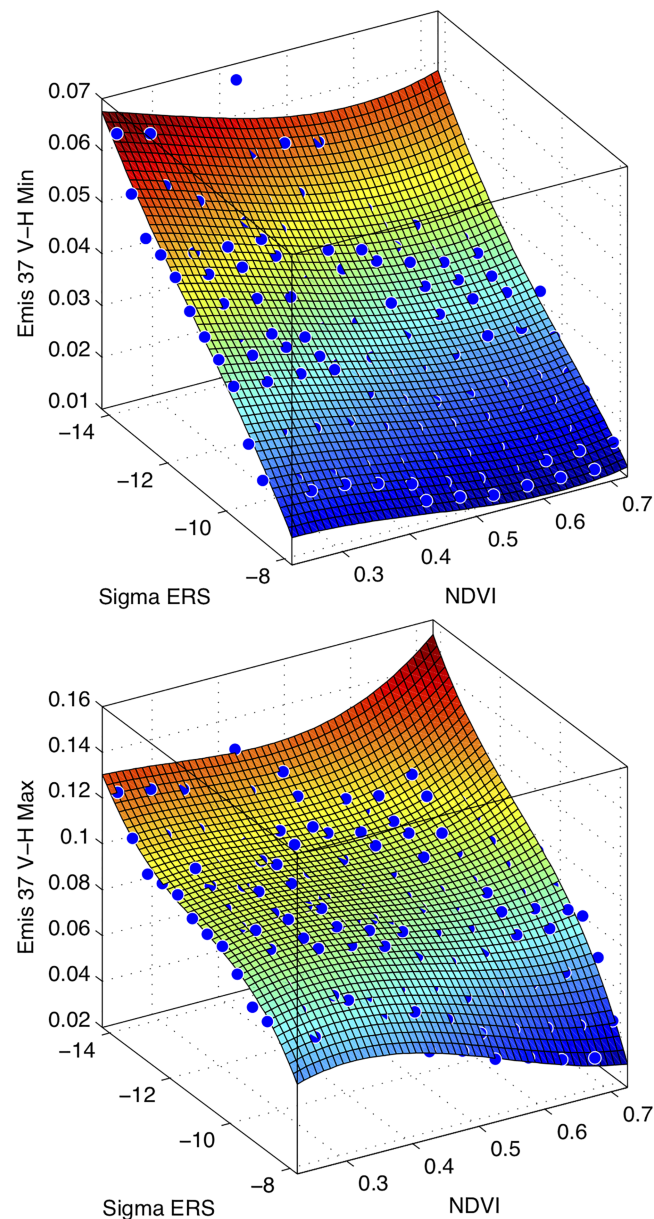
Figure 3. On the top (respectively on the bottom), the mean emissivity polarization difference at 37 GHz, for the 20% lowest (respectively highest) emissivity differences at 37 GHz, as a function of σ ERS and NDVI (the blue dots), along with the corresponding 2D polynomial fit, as calculated for 1 year of inundated pixels at global scale.

an 8-year monthly mean climatology of Advanced Very-High-Resolution Radiometer NDVI observations. These climatologies remain unchanged with respect to GIEMS-1 (see Papa et al., 2010 for details about their selection). The snow pixels are excluded from the classification, using a snow flag derived from the snow density and the snow depth from the ECMWF reanalysis (P. de Rosnay, ECMWF, personal communication, 09/2016). This snow flag replaces the one based on NSIDC snow information and used in GIEMS-1. Apart from the snow flag, this second step of the algorithm remains identical to the one applied in GIEMS-1 (Figure 2).

2.3. Quantification of the Surface Water Fraction per Pixel

The third and last step consists in calculating the fraction of surface water in the pixels once surface water is detected. The emissivity polarization difference at 37 GHz is particularly sensitive to the surface water fraction, but it is also modulated by vegetation. The emissivity polarization increases with surface

water fraction, but it declines with increasing vegetation density: the water and the vegetation contributions are mixed together in the signal. To disentangle the two contributions, a linear mixture model was adopted. In GIEMS-1, the scatterometer observations were used as a proxy for the vegetation. It was based on the fact that the microwave backscattering was not very sensitive to the presence of water and it increased with vegetation density (Prigent, Matthews, et al., 2001). For a given vegetation density (corresponding to a given backscattering coefficient), the pixels with low (respectively high) emissivity polarization difference at 37 GHz corresponded to low (respectively high) surface water fraction: the surface water fraction was assumed to vary linearly with the emissivity polarization difference between these extreme low and high vegetation densities.

Overestimation of the surface water percentage in GIEMS-1 was noticed by several users, especially for water surfaces covered by rather low vegetation, such as rice paddies. A first adjustment to the 2001 methodology was applied in 2010 (Papa et al., 2010), but more recent analyses showed that further adjustments were required. In surface water areas with low vegetation, the backscattering can be rather large, due to reflection of the radar signal on the water after bouncing back from plant stems (the so-called "double-bounce effect"). This high backscattering can be misinterpreted as representative of an area without any vegetation, and as a consequence, the surface water fraction can be overestimated. To avoid this problem, we propose to quantify the vegetation contribution using both the ERS backscattering (σ) and the NDVI. The backscattering and the NDVI are complementary information to characterize the vegetation contribution to the emissivity signal (their linear correlation coefficient is only 0.4 over these inundated pixels). Here, a new two-dimension linear mixture model is suggested, using both the σ ERS and the NDVI to characterize the vegetation contribution to the emissivity. Figure 3 (top panel) presents the mean emissivity polarization difference at 37 GHz, for the 20% lowest emissivity differences, as a function of σ ERS and NDVI (the blue dots), along with the polynomial surface fit to represent the relationship between these three variables. The same fitting is done for the 20% highest emissivity differences (bottom panel).

The next phase is to associate these low and high 20% values of the emissivity polarization differences to a given surface water fraction in order to establish a linear model for each σ ERS and NDVI bin relating the emissivity polarization difference to a surface water fraction. For each σ ERS and NDVI bin, the average of the 20% lowest values of the emissivity polarization differences at 37 GHz is affected to a 1% surface water fraction in the pixel, whereas the average of the 20% highest values of the emissivity polarization differences is affected to a 50% surface water fraction in the pixel. Here, we make an assumption on the global probability distribution of the surface water fraction. The global probability distribution of the lake size decreases as a power law, with a tail exponent of the order of 2 (Cael & Seekell, 2016). We expect the probability distribution of surface water extent to follow a similar law. The attribution of a 1% and 50% surface water fraction to the 20% lowest and highest values of emissivity polarization differences at 37 GHz respectively is compatible with this power law. Note that several tests were conducted to fine-tune these values, and the more realistic distribution of surface water extent at a global scale was obtained with these parameters.

3. Production of a Global Surface Water Extent Data Record

3.1. Global Results

The essential information used as input in this method, the passive microwave satellite observations from SSM/I and SSMIS, are available since 1992 up to now. It covers ~25 years with different instruments (SSM/I and SSMIS) on board several satellites (from F08 to F18). Figure 4 from Remote Sensing System (www.remss.com/support/crossing-times/) shows the ascending node crossing time for the different satellites. The change from the SSM/I series to the SSMIS between F15 and F16 corresponds to a significant modification of the instrument, with the addition of sounding channels as well as different observation strategies. These observations have recently been carefully intercalibrated at the Climate SAF and are provided to the community up to beginning of 2016 (Fennig et al., 2017). More recent data will be available soon.

Originally in GIEMS-1, all available satellite observations for a given month were included in the estimation of monthly emissivities, but for this new estimation of the emissivities we limit the observations to the F11, F13, and F17 platforms to get a consistent overpassing time close to 6 a.m. and 6 p.m. for all the measurements. Current research we are conducting shows that in some regions there can be a small but observable diurnal cycle in the emissivities, possibly linked to diurnal variations of the surface conditions (e.g., water in the plants, moisture in the soil), although inversion issues need also to be investigated (e.g., dependence
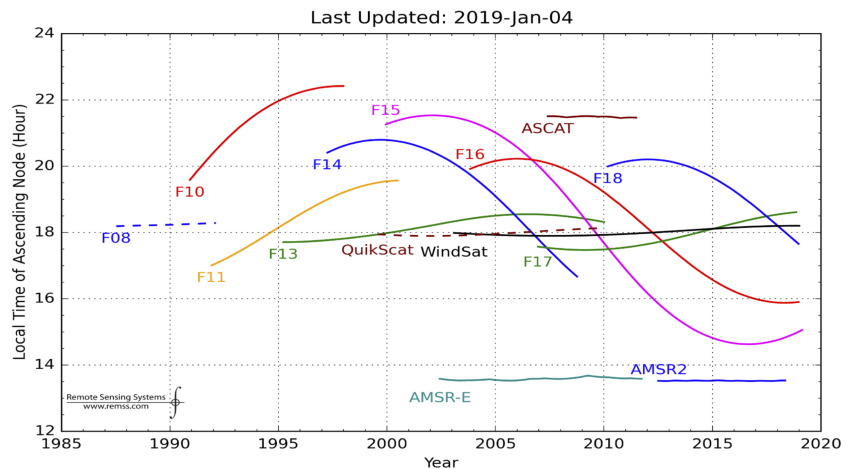
Figure 4. Local observing time of the DMSP satellites carrying SSM/I and SSMIS instruments (from Remote Sensing System http://www.remss.com/support/crossing-times/).

of the emissivity estimation on the assumed surface temperature). The F11, F13, and F17 satellites cover the 1992–2015 period with minimum time differences between observations. As shown in Figure 4, there are a few years of overlapping observations between F11 and F13 and a shorter period between F13 and F17. The current GIEMS-2 product includes estimations from F11, F13, and F17 covering respectively the 1992–1994, 1995–2008, and 2009–2015 periods, but full F11, F13, and F17 periods are internally processed to have overlapping periods allowing the analysis of any issues related to changes in the observing instruments. Both morning and afternoon observations are included in the estimation. The data are available on an equal area grid of 0.25° × 0.25° at the equator (∼25 km spatial resolution), with each pixel representing 773 km^2.

For the full data record, the surface water extent is estimated by using the algorithm described in section 2, that is, with the new emissivity methodology applied to the F11 and F13 SSM/I, and F17 SSMIS observations, together with the new surface water fraction calculation. The new emissivity estimation is also performed in pixels closely surrounding the locations that are inundated at least 1 month during the 1993–2007 original GIEMS-1 period. Given the very close surface conditions expected in the vicinity of these pixels, the emissivity estimation over the new surrounding pixels is still valid, and this allows some spatial variations in the inundated areas with respect to the original period. The two methodological changes (emissivity calculation and quantification of the surface water fraction) have been thoroughly tested separately. Only the final results are presented here.

For evaluation purposes, the same methodology is also applied to estimate surface water extent replacing the SSM/I brightness temperatures with observations from the Earth Observation Satellite Advanced Microwave Scanning Radiometer (AMSR-E). AMSR-E observations cover the period 2002–2011, therefore overlapping parts of the F13 SSM/I and F17 SSMIS data records. This provides a unique opportunity to test the possibly critical changes between the F13 and F17 instruments. We do not expect the AMSR-E derived surface water extent absolute values to perfectly match the SSM/I and SSMIS derived values, given the differences between both sensors, namely, the overpass times (1:30 a.m./p.m. for AMSR-E) and the higher ground resolution of AMSR-E (AMSR-E having roughly half of the SSM/I ground footprint). The latter is especially critical for the linear model calculating the surface water fraction, which has been fitted to the SSM/I observations. However, we expect the changes in the surface water extent to have similar relative temporal behavior and to produce reasonable agreement in the anomalies once the mean annual cycle is removed from the surface water extent estimations.

Figure 5 presents global maps of (1) the averaged surface water extent over the full time period (top), (2) the averaged annual maximum surface water extent (middle), and (3) the month of the maximum surface water extent in average (bottom). The major hydrological structures are clearly observed, with the expected temporal patterns, regardless of the environments, from the tropics to the poles. There are no obvious artifacts related to coastal contamination, spurious water detection in desert areas, nor evident underestimation in
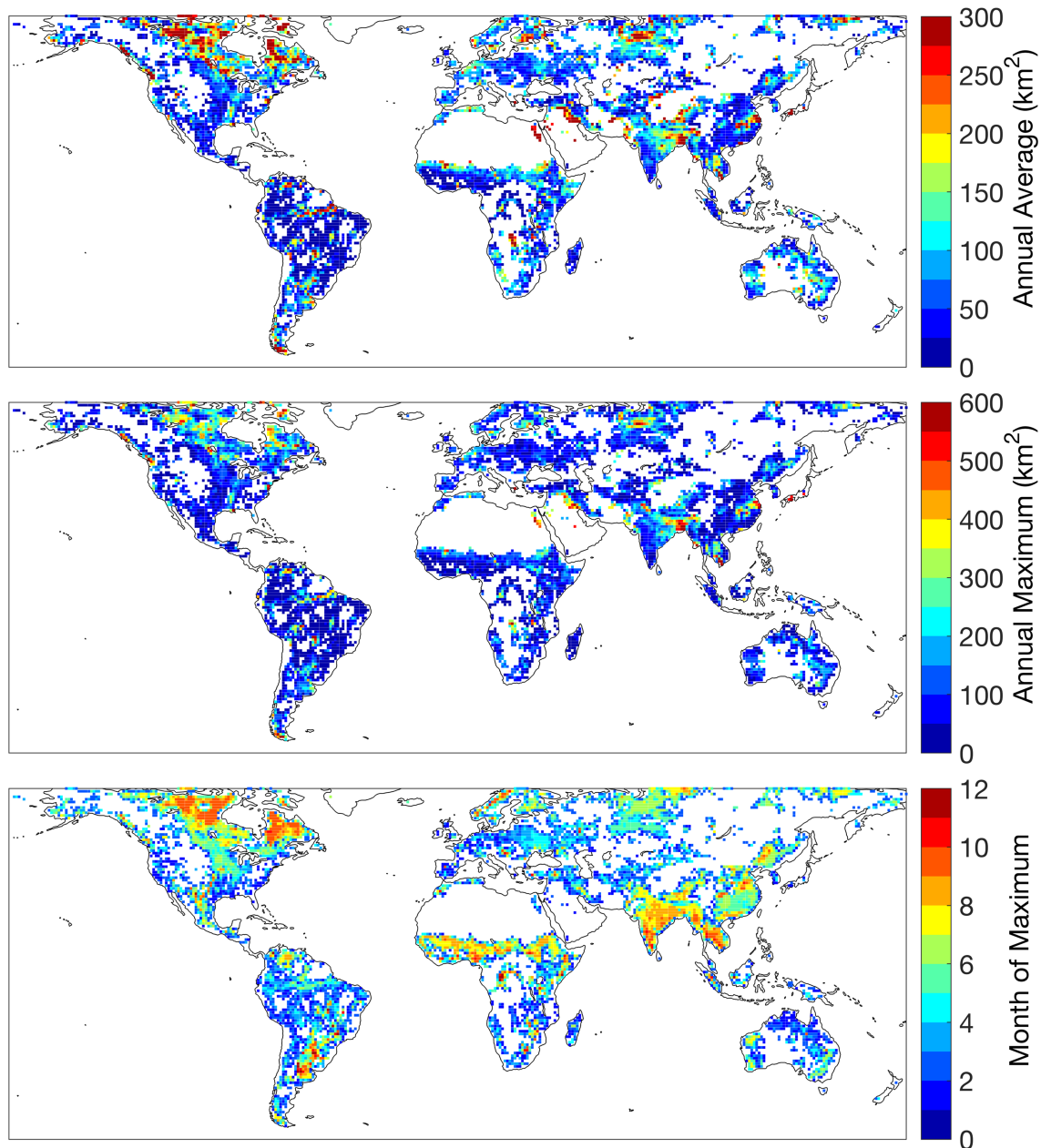
Figure 5. GIEMS-2 global maps of the averaged surface water extent over the full time period (top), the averaged annual maximum surface water extent (middle), and the month of the maximum surface water extent in average (bottom). The results are projected on an equal area grid of 773 km^2, calculated over the 1992–2015 period.

densely forested regions, as observed in other products (Pham-Duc, Prigent, Aires, & Papa, 2017). Note that large lakes have been excluded from the analysis.

3.2. Zonal Estimations

Time series of the zonal means of the surface water extent derived from the F11, F13, and F17 instruments are presented in Figure 6, along with the global results. Absolute values (top panels) and anomalies (bottom panels) are presented. The anomalies are calculated by removing from each sensor absolute value the zonal mean annual cycle estimated over the 1992–2015 period, that is, including the F11 (1992–1994), F13 (1995–2008), and F17 (2009–2015) records. The F11 and F13 overlapping period covers 4 years (1995–1999), and a good agreement between their respective anomalies can be observed. It is more difficult to judge for the F13 and F17 as there is only one common year (2008), but the anomalies are also in
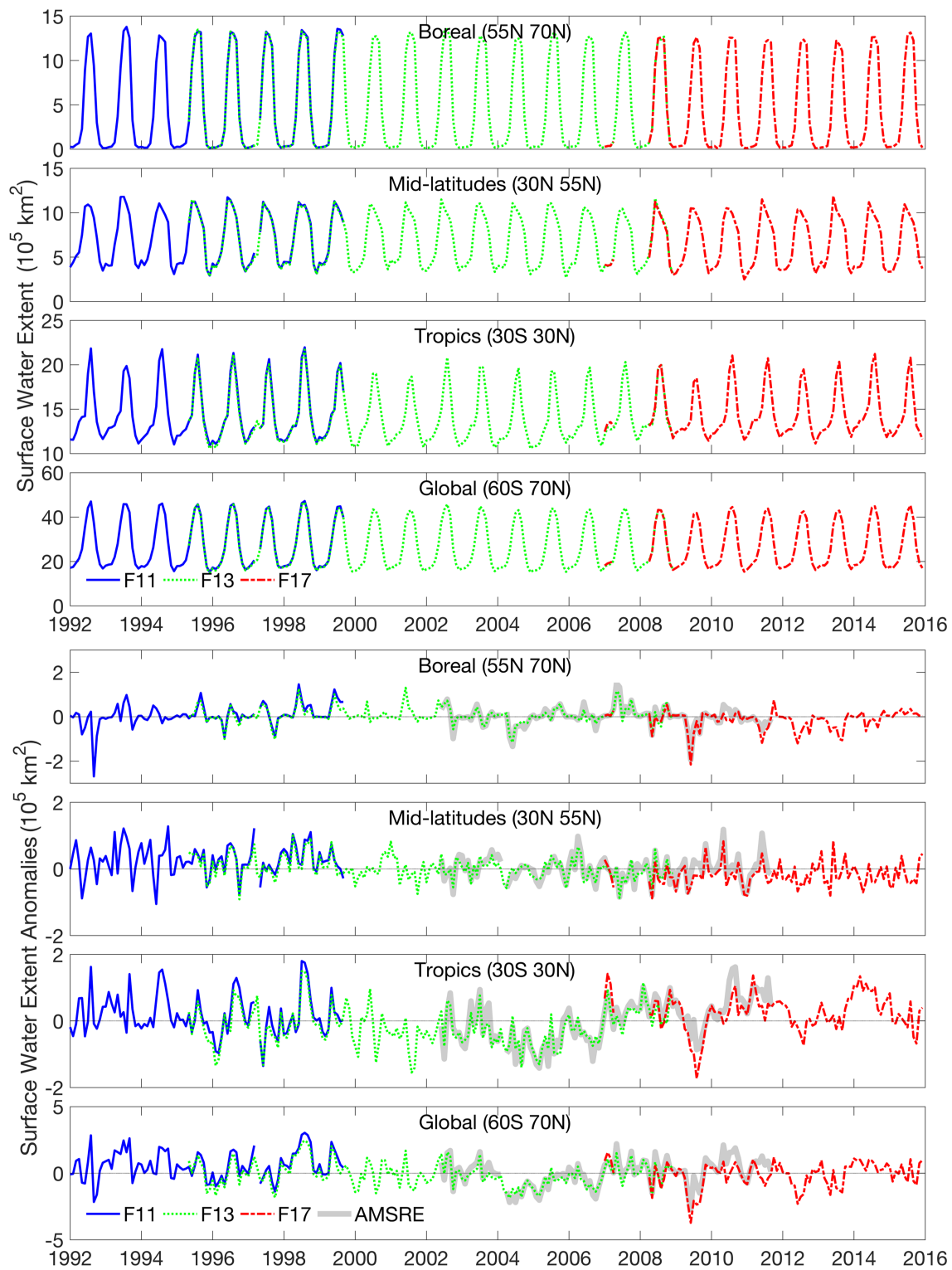
Figure 6. Zonally integrated time series of the surface water extent (top) and their anomalies (bottom), for different latitudinal bands and for the globe, separating the F11, F13, and F17 records. The AMSR-E anomalies are also added. See text for details.
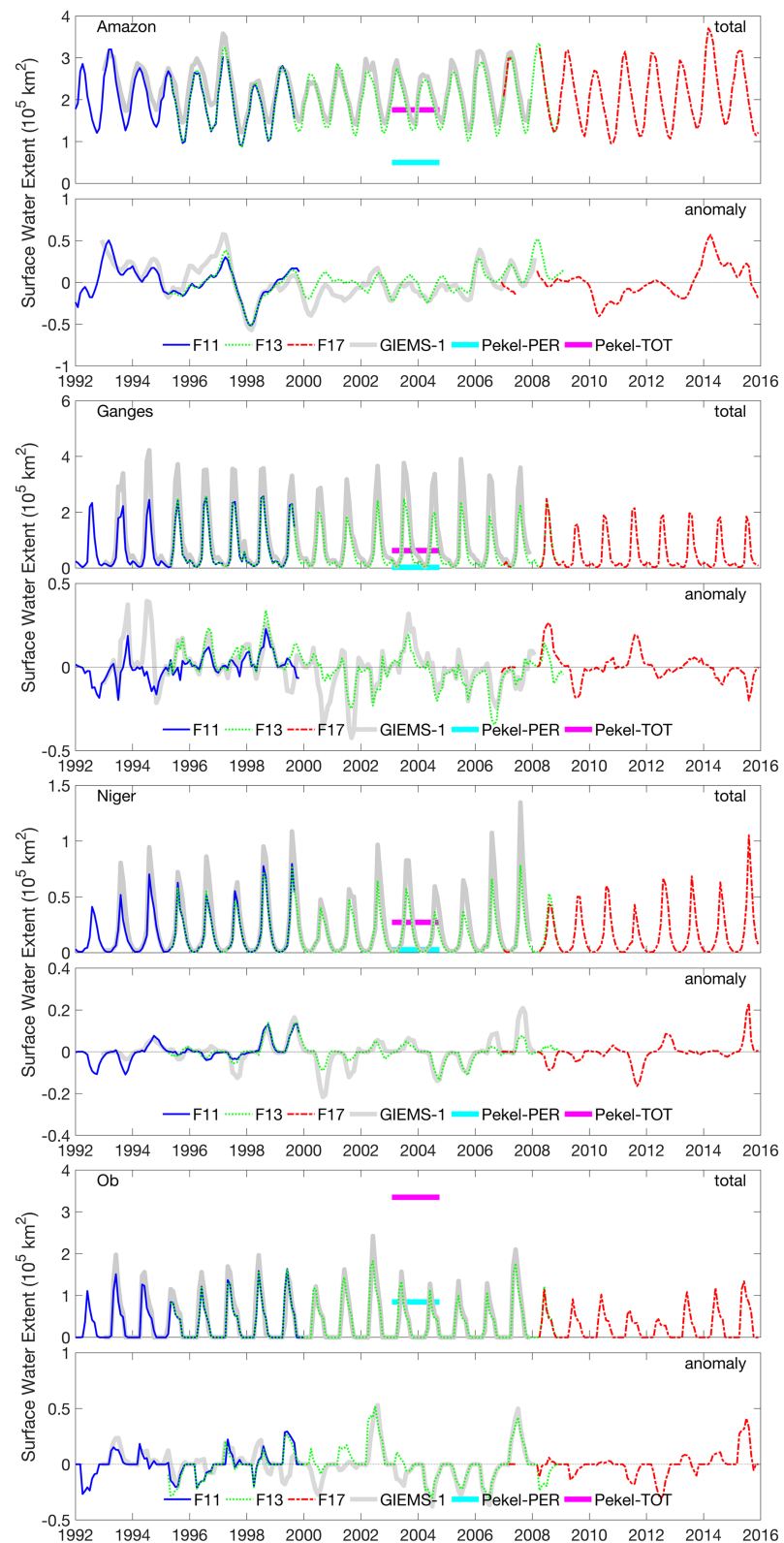
Figure 7. From top to bottom: Spatially integrated time series of the GIEMS-2 surface water extent and their anomalies for the Amazon, the Ganges, the Niger, and the Ob. Anomalies are calculated as in Figure 6. The permanent surface water extent estimated by Pekel et al. (2016) is also indicated, along with their total water extent at maximum (permanent plus transitory surface water extents).

good agreement. This gives confidence in the production of a seamless continuous data record with limited impacts related to intersensor differences. The anomalies are also presented for the overlapping period between F13, F17, and AMSR-E. Note that the F17 and F13 anomalies are calculated with the full GIEMS-2 data record, while AMSR-E anomalies are estimated by removing its own zonal mean annual cycle estimated over the 2002–2011 period. This minimizes the impact of AMSR-E having relatively large surface water extent biases with respect to GIEMS-2, as previously discussed (section 3.1). The agreement between the different anomalies is very satisfying, implying that, at least across large spatial scales, GIEMS-2 does not present obvious artifacts related to the change from SSM/I to SSMIS. Both seasonal cycles and year-to-year variations of inundated areas are found to be the largest in the tropical band. Decreasing (e.g., 1998–2005) and increasing (e.g., 2005–2011) long-term trends are visible in the tropics but not for other latitudes (Figure 6, bottom). Such variations are consistent with wetland extent playing a role in the understanding of atmospheric methane variations in the past decades (e.g., Bousquet et al., 2006; Nisbet et al., 2016; Saunois et al., 2017; Thompson et al., 2018).

3.3. Basin Estimations

Spatially integrated time series of the F11, F13, F17, and GIEMS-1 surface water extent values and anomalies are plotted for the Amazon, Ganges, Niger, and Ob basins, in Figure 7. For all the basins, regardless of the environments, the F11 and F13 (respectively F13 and F17) estimates agree very well over their common periods, not only in absolute values but also in their anomalies, which is much more demanding. GIEMS-1 and GIEMS-2 show obvious differences, as the evolution from GIEMS-1 to GIEMS-2 solved known problems with GIEMS-1. For instance, over the Ganges and the Niger, GIEMS-2 produces less surface water extent than GIEMS-1, as expected and as already discussed in section 2.3. Nevertheless, the interannual behavior is maintained, with very good agreement in the anomalies between GIEMS-1 and GIEMS-2.

Pekel et al. (2016) used a very large number of Landsat images over more than 30 years to produce the Global Surface Water Occurrence at 30-m spatial resolution. From this data set, the permanent and the transitory surface water maps are derived, and we projected it on the GIEMS-2 grid. For each selected basin, the permanent surface water extent estimated by Pekel et al. (2016) is added to Figure 7 (Pekel-PER), along with the total water extent (permanent plus transitory) at maximum (Pekel-TOT). We would expect the permanent surface water extent from Pekel et al. (2016) to be close to the minimum value of GIEMS in the annual cycle, and the total surface water extent close to the maximum GIEMS annual value. Note that the considered time period for Pekel et al. (2016) is larger than our record. The comparisons with the Pekel et al. (2016) estimates confirm the significant differences between the two estimates: the visible method usually underestimates the surface water extent in region of large vegetation cover. This is true under tropical forest but also under dense low vegetation as in the Niger Delta or in the Ganges region, during the wet season. The maximum extent of the surface water can also be difficult to capture with such observations, as the maximum surface water extent tends to coincide with the maximum cloud cover. However, we are also aware that our methodology can overestimate the surface water extent, as it is also sensitive to very saturated soil. In the Ob basin, GIEMS-2 observes less surface water than Pekel et al. (2016), and this will require further investigation. Note that over boreal basins, Pekel et al. (2016) information might be only relevant during summer, as no visible observation is collected during the polar night.

4. Evaluation of the Time Record of Global Surface Water Extent

4.1. Comparisons With Precipitation

We now compare GIEMS-2 surface water extent and the precipitation estimates from the Multi-Source Weighted-Ensemble Precipitation (MSWEP) version 1 product (Beck et al., 2017). This product combines gauge, satellite, and reanalysis data and is broadly used to provide global estimates of precipitation for hydrological modeling. It includes both rain and snow estimates.

Figure 8 displays Hovmöller diagrams of the surface water extent and precipitation anomalies. A 3-month running mean is applied to smooth the distributions. Only precipitation over cells that are inundated at least once during the considered 1992–2015 period is included in the zonal averages. In general, a relatively good agreement in the interannual variability of surface water extent and precipitation is found at tropical latitudes, with a much worse agreement at higher latitudes. Flooding can occur in response to locally intense precipitation as well as to snow melt or to heavy precipitation in upstream locations. In the tropics, surface water is essentially related to precipitation, and the close agreement in the patterns of the anomalies in surface water extent and precipitation gives confidence in the interannual variability of our surface water extent
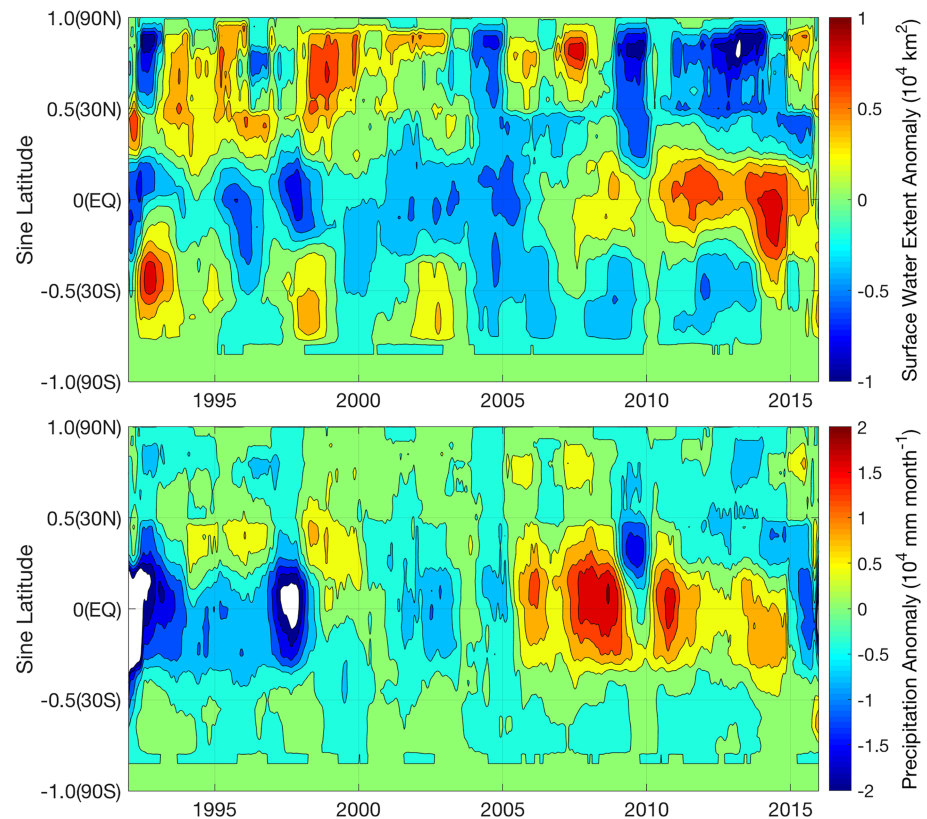
Figure 8. Hovmöller diagrams of the anomalies of the surface water extent (top) and precipitation (bottom).

estimation. At high latitudes, surface water essentially results from the snow melt, not from precipitation, liquid or solid, explaining the low correlation between surface water and precipitation.

The patterns can also be explained by the different relationships between surface water and precipitation depending on the averaged surface conditions and precipitation regimes for a given latitudinal band. The surface water characteristics depend on the distribution and intensity of precipitation as well as on the land surface properties that control how precipitation is partitioned among evaporation, storage at the surface and at depth, and runoff. Figure 9 shows the maximum correlation and corresponding time lag in months between surface water extent and precipitation. A positive (respectively negative) time lag indicates that the presence of surface water follows (respectively precedes) precipitation. The presence of surface water and precipitation can be separated in both time and space, with significant time lags between maximum surface water extent and precipitation. The linear correlation is large in regions with strong precipitation seasonal cycles with direct impact on the surface water (no time lag), such as in Southeast Asia where the monsoon regime dominates the precipitation cycle and the related surface water. As mentioned above, boreal wetlands are essentially due to snow melting, and as a consequence, their extent is less correlated with the precipitation rate (e.g., the Ob region in Russia). In other regions, such as the Amazon, the surface water can be produced by precipitation upstream, and a significant systematic lag can be observed between the local precipitation and the surface water.

4.2. Comparisons With River Height From Satellite Altimeters

Surface water extent and water height are strongly related. Combined together, these two parameters can provide an estimate of the water storage in the floodplains (e.g., Frappart et al., 2008, 2012; Papa et al., 2015). Here, the water levels are extracted from the Surfaces Continentales Théia Projet HYDROWEB (hydroweb.theia-land.fr). It provides the water height over rivers and lakes, all over the globe, from a collection of satellite altimeters covering a long period of time (Da Silva et al., 2010; Normandin et al., 2018). Consistent data from the Jason altimeter have been collected from 2008 to 2016, close to the mouth of the river, for several basins. Figure 10 shows a comparison of the time series of basin integrated surface water
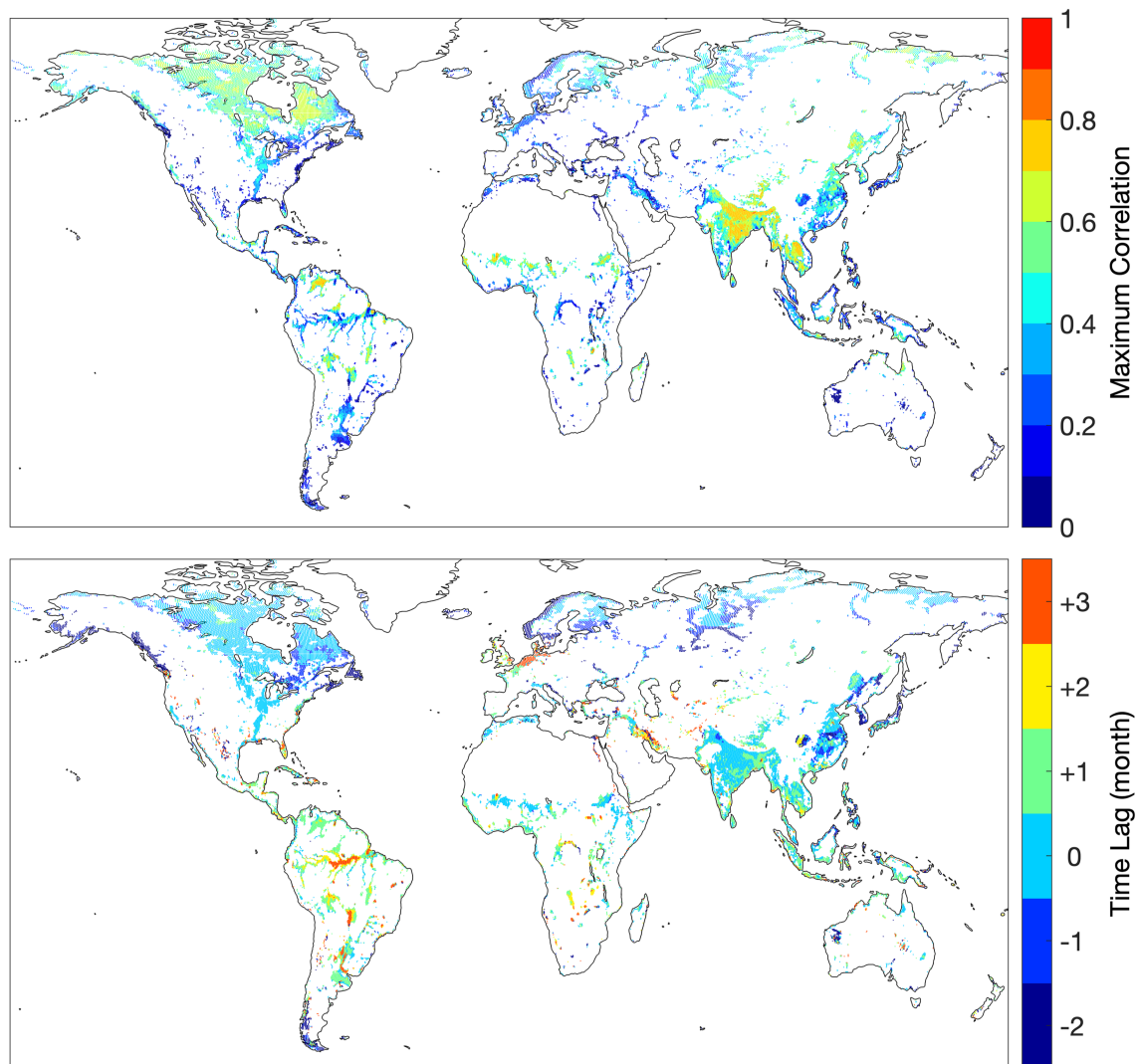
Figure 9. Temporal correlation between the GIEMS-2 surface water extent and MSWEP precipitation. The maximum correlation (top) and corresponding time lag in months (bottom) are displayed.

extent, the basin integrated precipitation (presented in section 4.1), and a mean water level obtained by averaging the individual values at the available locations along the main stream, close to the mouth of the basin. For comparison purposes, the time series are standardized for each product; that is, the mean is subtracted and the resulting values are divided by the standard deviation over the period.

There is a general good agreement between the interannual variations of the altimeter river height and the surface water extent over this time period, with also good relationship with the precipitation. The major features are captured by the three products, such as the significant decrease in 2009 in the Orinoco and Brahmaputra basins, corresponding to an El Niño event (e.g., Khandu et al., 2016). For the Orinoco and Brahmaputra basins, precipitation precedes the increase in surface water extent, as already discussed in section 4.1. However, some significant differences are observed locally such as the rapid increase of precipitation and surface water extent middle of 2015 over the Niger basin but without any related changes in the altimetry data or the large variability in the altimetry signal in 2015 over the Orinoco basin, and without any counterpart on the two other hydrological parameters. This is partly related to the way the altimeter water height has been processed. The altimeter water estimates are not available all over the basins but at a few locations along the river. Here, we average different points at the mouth of the river and provide the highest and lowest values. The averaged information, although hydrologically related to the surface water extent,
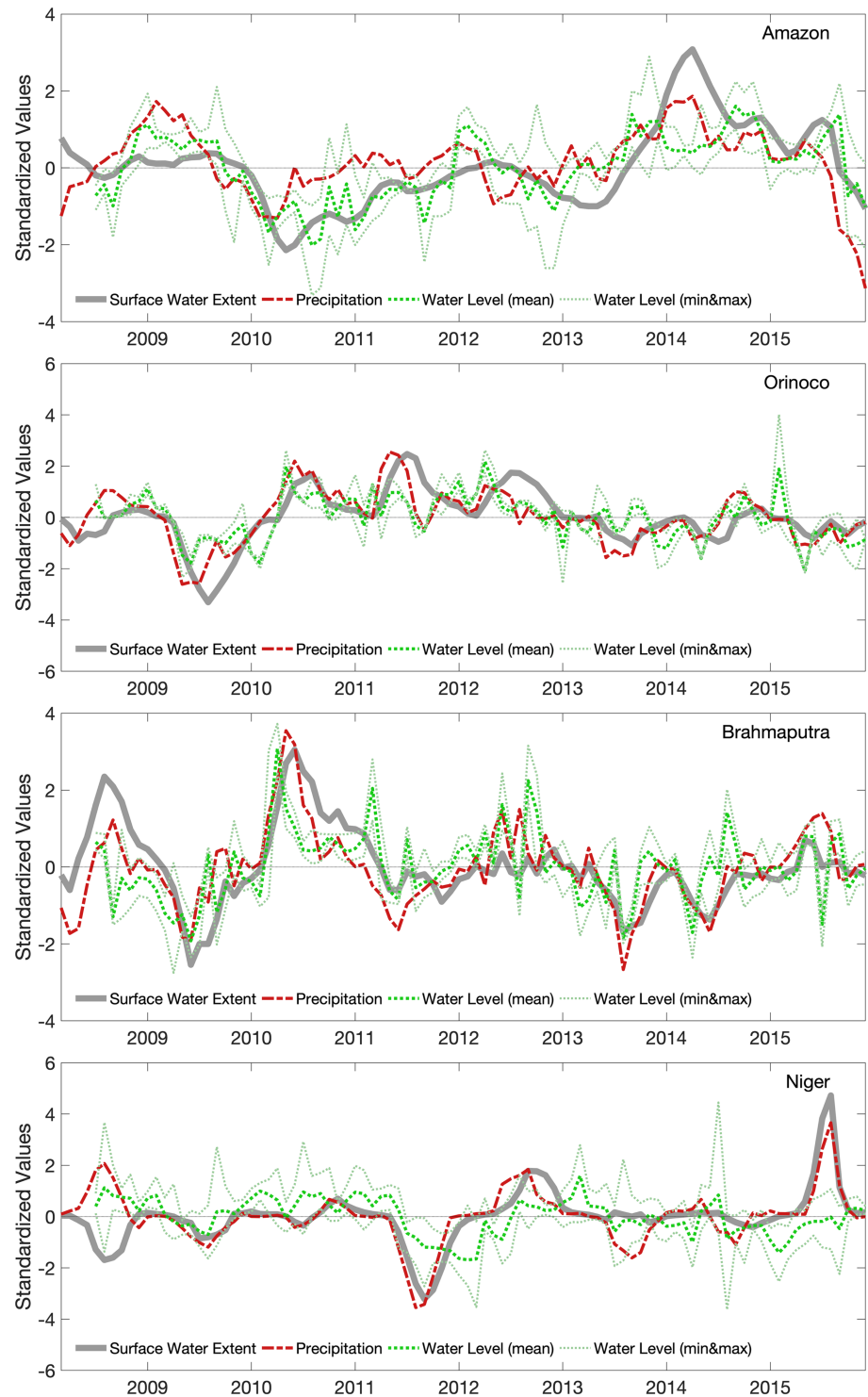
Figure 10. Comparison of time series of standardized basin integrated GIEMS-2 surface water extent, basin integrated MSWEP precipitation, and mean altimetric water levels at the mouth of the basins from HYDROWEB, along with the highest and lowest water levels in the area.

might not always be representative of the entire basin hydrological variability, depending on the location of the available altimeter points.

5. Conclusion

A method has been developed to extend the original GIEMS surface water data record (Papa et al., 2010; Prigent, Matthews, et al., 2001; Prigent et al., 2007). The new product, GIEMS-2, provides monthly mean surface water extent globally from 1992 to 2015 on an equal area grid of 0.25° × 0.25° at the equator (~25 km spatial resolution or 773 km^2). It comprises all surface waters, including open water, wetlands, or rice paddies. The time series have been thoroughly evaluated: they are seamless and do not show any obvious artifact related to changes in satellite instrumentation over the ~25 years.

Downscaling methodologies have been developed from GIEMS-1 to provide the user community with down to 90 m resolution estimates, using topography information from digital elevation models, to provide a global consistent reference data set on water surfaces, at high spatial resolution (Aires et al., 2017, 2018; Fluet-Chouinard et al., 2015). It can complement the local independent current estimates, with a reference that is suitable at large scale, for applications such as risk management or pricing of insurance policies. Similar downscaling methodologies are planned for GIEMS-2. Further work is also taking place to improve the GIEMS-2 temporal resolution, with a 10-day data record over the same period of time currently under construction.

Wetlands are a major source of atmospheric methane and the only one dominated by climate. Analysis of the GIEMS-2 record is underway to help understand the methane atmospheric variability over the last 25 years. It will include direct comparison with in situ atmospheric methane concentration as well as evaluation through methane emission simulations.

GIEMS-2 production will be systematically continued, as soon as the SSMIS data are available from the EUMETSAT Climate SAF. There is currently no plan to launch any new SSMIS instruments, once the current ones end. Continuity of AMSR data is still under discussion. On the European side, the next generation of meteorological satellites (MetOp-SG) to be launched in 2020 will be equipped with a conical scanner, the MicroWave Imager, that will include the SSMIS window channels (D'Addio et al., 2014). This will make it possible to extend the GIEMS-2 time series. In addition, within the Copernicus framework, a conical scanner with frequencies between 1.4 and 36 GHz (the Copernicus Imaging Microwave Radiometer, CIMR) is under consideration, with much improved spatial resolution, ~5 km at 18 and 36 GHz, thanks to a large antenna of the order of 7 m diameter (Kilic et al., 2018).

The NASA/CNES Surface Water and Ocean Topography mission, planned for launch in 2021, is specifically designed to provide high spatial resolution and temporal sampling of the area (and height) of continental surface waters (Biancamaria et al., 2016; Prigent et al., 2016) thanks to an interferometric Ka-band radar (Fu et al., 2012). Meanwhile, alternative efforts should be pursued to provide the community with the best possible information about the spatial and temporal variations of the global surface water extents. Such efforts would also allow for extending the Surface Water and Ocean Topography time record backward with existing past imagery, and it will be a crucial step in assembling multidecadal measurements of surface water variations.

References

Aires, F., Miolane, L., Prigent, C., Pham, B., Fluet-Chouinard, E., Lehner, B., & Papa, F. (2017). A global dynamic long-term inundation extent dataset at high spatial resolution derived through downscaling of satellite observations. *Journal of Hydrometeorology*, *18*(5), 1305–1325. https://doi.org/10.1175/JHM-D-16-0155.1

Aires, F., Prigent, C., Bernardo, F., Jiménez, C., Saunders, R., & Brunel, P. (2011). A Tool to Estimate Land-Surface Emissivities at Microwave frequencies (TELSEM) for use in numerical weather prediction. *Quarterly Journal of the Royal Meteorological Society*, *137*(656), 690–699. https://doi.org/10.1002/qj.803

Aires, F., Prigent, C., Fluet-Chouinard, E., Yanazaki, D., Papa, F., & Lehner, B. (2018). Comparison of visible and multi-satellite global inundation datasets at high-spatial resolution. *Remote Sensing of Environment*, *216*, 427–441. https://doi.org/10.1016/j.rse.2018.06.015

Aires, F., Prigent, C., Rossow, W., & Rothstein, M. (2001). A new neural network approach including first guess for retrieval of atmospheric water vapor, cloud liquid water path, surface temperature, and emissivities over land from satellite microwave observations. *Journal of Geophysical Research*, *106*(D14), 14,887–14,907. https://doi.org/10.1029/2001JD900085

Alsdorf, D. E., Rodríguez, E., & Lettenmaier, D. P. (2007). Measuring surface water from space. *Reviews of Geophysics*, *45*, RG2002. https://doi.org/10.1029/2006RG000197

Beck, H. E., Van Dijk, A. I., Levizzani, V., Schellekens, J., Gonzalez Miralles, D., Martens, B., & De Roo, A. (2017). Mswep: 3-hourly 0.25 global gridded precipitation (1979–2015) by merging gauge, satellite, and reanalysis data. *Hydrology and Earth System Sciences*, *21*(1), 589–615. https://doi.org/10.5194/hess-21-589-2017

Biancamaria, S., D. P. Lettenmaier, and T. M. Pavelsky (2016). The swot mission and its capabilities for land hydrology. In *Remote Sensing and Water Resources* (pp. 117–147). Springer. https://doi.org/10.1007/978-3-319-32449-4_6.

Bousquet, P., Ciais, P., Miller, J., Dlugokencky, E. J., Hauglustaine, D., Prigent, C., et al. et al. (2006). Contribution of anthropogenic and natural sources to atmospheric methane variability. *Nature*, *443*(7110), 439–443. https://doi.org/10.1038/nature05132

Cael, B. B., & Seekell, D. A. (2016). The size-distribution of Earth's lakes. *Scientific Reports*, *6*(1), 29633. https://doi.org/10.1038/srep29633

D'Addio, S., V. Kangas, U. Klein, M. Loiselet, and G. Mason (2014). The microwave radiometers on-board metop second generation satellites. In *Metrology for Aerospace (MetroAeroSpace)* (pp. 599–604). IEEE.

Da Silva, J. S., Calmant, S., Seyler, F., Rotunno Filho, O. C., Cochonneau, G., & Mansur, W. J. (2010). Water levels in the Amazon basin derived from the ERS 2 and Envisat radar altimetry missions. *Remote Sensing of Environment*, *114*(10), 2160–2181. https://doi.org/10.1016/j.rse.2010.04.020

Dee, D. P., Uppala, S. M., Simmons, A. J., Berrisford, P., Poli, P., Kobayashi, S., et al. (2011). The ERA-Interim reanalysis: Configuration and performance of the data assimilation system. *Quarterly Journal of the Royal Meteorological Society*, *137*(656), 553–597. https://doi.org/10.1002/qj.828

Fennig, K., M. Schroder, and R. Hollmann (2017). Fundamental climate data record of microwave imager radiances, Tech. rep., Satellite Application Facility on Climate Monitoring, EUMETSAT.

Fluet-Chouinard, E., Lehner, B., Rebelo, L.-M., Papa, F., & Hamilton, S. K. (2015). Development of a global inundation map at high spatial resolution from topographic downscaling of coarse-scale remote sensing data. *Remote Sensing of Environment*, *158*, 348–361. https://doi.org/10.1016/j.rse.2014.10.015

Frappart, F., Papa, F., da Silva, J. S., Ramillien, G., Prigent, C., Seyler, F., & Calmant, S. (2012). Surface freshwater storage and dynamics in the Amazon basin during the 2005 exceptional drought. *Environmental Research Letters*, *7*(4), 044,010. https://doi.org/10.1088/1748-9326/7/4/044010

Frappart, F., Papa, F., Famiglietti, J. S., Prigent, C., Rossow, W. B., & Seyler, F. (2008). Interannual variations of river water storage from a multiple satellite approach: A case study for the Rio Negro river basin. *Journal of Geophysical Research*, *113*, D21104. https://doi.org/10.1029/2007JD009438

Fu, L.-L., D. Alsdorf, R. Morrow, E. Rodriguez, and N. Mognard (2012). SWOT: The Surface Water and Ocean Topography mission: Wide-swath altimetric elevation on Earth, Tech. rep., Jet Propulsion Laboratory, National Aeronautics and Space Agency, Pasadena, CA, USA.

Hagan, M. T., & Menhaj, M. B. (1994). Training feedforward networks with the Marquardt algorithm. *IEEE Transactions on Neural Networks*, *5*(6), 989–993. https://doi.org/10.1109/72.329697

Khandu, K., Forootan, E., Schumacher, M., Awange, J. L., Schmied, H. M., et al. (2016). Exploring the influence of precipitation extremes and human water use on total water storage (TWS) changes in the Ganges-Brahmaputra-Meghna River basin. *Water Resources Research*, *52*, 2240–2258. https://doi.org/10.1002/2015WR018113

Kilic, L., Prigent, C., Aires, F., Boutin, J., Heygster, G., Tonboe, R. T., et al. (2018). Expected performances of the Copernicus Imaging Microwave Radiometer (CIMR) for an all-weather and high spatial resolution estimation of ocean and sea ice parameters. *Journal of Geophysical Research: Oceans*, *123*, 7564–7580. https://doi.org/10.1029/2018JC014408

Kirschke, S., Bousquet, P., Ciais, P., Saunois, M., Canadell, J. G., Dlugokencky, E. J., et al. (2013). Three decades of global methane sources and sinks. *Nature Geoscience*, *6*(10), 813–823. https://doi.org/10.1038/ngeo1955

Melton, J. R., Wania, R., Hodson, E. L., Poulter, B., Ringeval, B., Spahni, R., et al. (2013). Present state of global wetland extent and wetland methane modelling: Conclusions from a model inter-comparison project (WETCHIMP). *Biogeosciences*, *10*(2), 753–788. https://doi.org/10.5194/bg-10-753-2013

Nisbet, E., Dlugokencky, E., Manning, M., Lowry, D., Fisher, R., France, J., et al. et al. (2016). Rising atmospheric methane: 2007–2014 growth and isotopic shift. *Global Biogeochemical Cycles*, *30*, 1356–1370. https://doi.org/10.1002/2016GB005406

Nisbet, E., Manning, M., Dlugokencky, E., Fisher, R., Lowry, D., Michel, S., et al. et al. (2018). Very strong atmospheric methane growth in the four years 2014–2017: Implications for the Paris agreement. *Global Biogeochemical Cycles*, *33*, 318–342. https://doi.org/10.1029/2018GB006009

Normandin, C., Frappart, F., Diepkilé, A. T., Marieu, V., Mougin, E., Blarel, F., et al. (2018). Evolution of the performances of radar altimetry missions from ERS-2 to Sentinel-3a over the inner Niger Delta. *Remote Sensing*, *10*(6), 833. https://doi.org/10.3390/rs10060833

Papa, F., Frappart, F., Malbeteau, Y., Shamsudduha, M., Vuruputur, V., Sekhar, M., et al. (2015). Satellite-derived surface and sub-surface water storage in the Ganges–Brahmaputra River basin. *Journal of Hydrology: Regional Studies*, *4*, 15–35.

Papa, F., Prigent, C., Aires, F., Jimenez, C., Rossow, W., & Matthews, E. (2010). Interannual variability of surface water extent at the global scale, 1993–2004. *Journal of Geophysical Research*, *115*, D12111. https://doi.org/10.1029/2009JD012674

Pekel, J.-F., Cottam, A., Gorelick, N., & Belward, A. S. (2016). High-resolution mapping of global surface water and its long-term changes. *Nature*, *540*(7633), 418–422. https://doi.org/10.1038/nature20584

Pham-Duc, B., Prigent, C., & Aires, F. (2017). Surface water monitoring within Cambodia and the Vietnamese Mekong Delta over a year, with Sentinel-1 SAR observations. *Water*, *9*(6), 366. https://doi.org/10.3390/w9060366

Pham-Duc, B., Prigent, C., Aires, F., & Papa, F. (2017). Comparisons of global terrestrial surface water datasets over 15 years. *Journal of Hydrometeorology*, *18*(4), 993–1007. https://doi.org/10.1175/JHM-D-16-0206.1

Pison, I., Ringeval, B., Bousquet, P., Prigent, C., & Papa, F. (2013). Stable atmospheric methane in the 2000s: Key-role of emissions from natural wetlands. *Atmospheric Chemistry and Physics*, *13*(23), 11,609–11,623. https://doi.org/10.5194/acp-13-11609-2013

Prigent, C., Aires, F., Rossow, W., & Matthews, E. (2001). Joint characterization of vegetation by satellite observations from visible to microwave wavelengths: A sensitivity analysis. *Journal of Geophysical Research*, *106*(D18), 20,665–20,685. https://doi.org/10.1029/2000JD900801

Prigent, C., D. P. Lettenmaier, F. Aires, and F. Papa (2016). Toward a high-resolution monitoring of continental surface water extent and dynamics, at global scale: From GIEMS (Global Inundation Extent from Multi-satellites) to SWOT (Surface Water Ocean Topography). In *Remote Sensing and Water Resources* (pp. 149–165). Springer. https://doi.org/10.1007/978-3-319-32449-4_7.

Prigent, C., Matthews, E., Aires, F., & Rossow, W. B. (2001). Remote sensing of global wetland dynamics with multiple satellite data sets. *Geophysical Research Letters*, *28*(24), 4631–4634. https://doi.org/10.1029/2001GL013263

Prigent, C., Papa, F., Aires, F., Jimenez, C., Rossow, W., & Matthews, E. (2012). Changes in land surface water dynamics since the 1990s and relation to population pressure. *Geophysical Research Letters*, *39*, L08403. https://doi.org/10.1029/2012GL051276

Prigent, C., Papa, F., Aires, F., Rossow, W., & Matthews, E. (2007). Global inundation dynamics inferred from multiple satellite observations, 1993–2000. *Journal of Geophysical Research*, *112*, D12107. https://doi.org/10.1029/2006JD007847

Prigent, C., Rossow, W. B., & Matthews, E. (1997). Microwave land surface emissivities estimated from SSM/I observations. *Journal of Geophysical Research*, *102*(D18), 21,867–21,890. https://doi.org/10.1029/97JD01360

Ringeval, B., De Noblet-Ducoudré, N., Ciais, P., Bousquet, P., Prigent, C., Papa, F., & Rossow, W. B. (2010). An attempt to quantify the impact of changes in wetland extent on methane emissions on the seasonal and interannual time scales. *Global Biogeochemical Cycles*, *24*, GB2003. https://doi.org/10.1029/2008GB003354

Rossow, W. B., & Schiffer, R. A. (1999). Advances in understanding clouds from ISCCP. *Bulletin of the American Meteorological Society*, *80*(11), 2261–2287. https://doi.org/10.1175/1520-0477(1999)080<2261:AIUCFI>2.0.CO;2

Rumelhart, D. E., G. E. Hinton, and R. J. Williams (1986). Learning internal representations by error propagation. In *Parallel distributed processing: Explorations in the microstructure of cognition, vol. I*, edited by D. E. Rumelhart, J. L. McClelland, and the PDP Research Group (pp. 318–362).Cambridge, MA: MIT Press.

Santoro, M., Wegmuller, U., Lamarche, C., Bontemps, S., Defourny, P., & Arino, O. (2015). Strengths and weaknesses of multi-year Envisat ASAR backscatter measurements to map permanent open water bodies at global scale. *Remote Sensing of Environment*, *171*, 185–201. https://doi.org/10.1016/j.rse.2015.10.031

Saunois, M., Bousquet, P., Poulter, B., Peregon, A., Ciais, P., Canadell, J. G., et al. (2017). Variability and quasi-decadal changes in the methane budget over the period 2000–2012. *Atmospheric Chemistry and Physics*, *17*(18), 11,135–11,161. https://doi.org/10.5194/acp-17-11135-2017

Schroeder, R., McDonald, K. C., Chapman, B. D., Jensen, K., Podest, E., Tessler, Z. D., et al. (2015). Development and evaluation of a multi-year fractional surface water data set derived from active/passive microwave remote sensing data. *Remote Sensing*, *7*(12), 16,688–16,732. https://doi.org/10.3390/rs71215843

Thompson, R. L., Nisbet, E., Pisso, I., Stohl, A., Blake, D., Dlugokencky, E., et al. (2018). Variability in atmospheric methane from fossil fuel and microbial sources over the last three decades. *Geophysical Research Letters*, *45*, 11,499–11,508. https://doi.org/10.1029/2018GL078127

Wania, R., Melton, J., Hodson, E., Poulter, B., Ringeval, B., Spahni, R., et al. et al. (2013). Present state of global wetland extent and wetland methane modelling: Methodology of a model inter-comparison project (WETCHIMP). *Geoscientific Model Development*, *6*(3), 617–641. https://doi.org/10.5194/gmd-6-617-2013